

# Machine Learning Based Evaluation of Surface Roughness of Additively- Manufactured Nylon 12 Surgical Guides

A. Pressly, J. Simsiriwong, G. May

College of Computing, Engineering, and Construction,  
University of North Florida, Jacksonville, FL, 32224

## Abstract

This study investigates the influence of fused deposition modeling (FDM) printing parameters and post-processing on the surface roughness of Nylon 12 specimens across two distinct collection sites. A machine learning methodology, incorporating Random Forest Regression alongside analytical tools such as correlation matrices, feature importance metrics, mutual information, and Analysis of Variance (ANOVA), was employed to model and correlate relationships between feature and target variables. The research revealed significant discrepancies in surface roughness characteristics between the two sites, with Site B consistently exhibiting a rougher surface topography. The predictive model developed for Site A demonstrated higher accuracy, with an R<sup>2</sup> value of 0.879, when compared to models developed for Site B and a combined dataset. Key printing parameters, specifically orientation, body thickness, and infill pattern, were identified as exerting substantial influence on the surface roughness of both sites. These findings emphasize that the optimization of surface quality requires a comprehensive understanding of printing parameters and processing conditions.

Keywords: Nylon12, FDM, Surface roughness, Random Forest Regression, 3D-printing optimization, ANOVA, Feature importance, Machine learning.

## 1. Introduction

The world of additive manufacturing (AM) consists of numerous types of object-making methods, namely three-dimensional printing. The growth of the AM industry is in part due to fused deposition modeling (FDM), which is one of the most popular forms of AM in various industries. Economic research predicts that the FDM market will experience more than a 30% growth by 2030 [1]. The growth of FDM is in part due to continuous research on printing materials, machines, and methods, which have become increasingly optimized to provide cost-effective, sustainable results [2, 3].

However, a bottleneck of new materials and the volume of printing process parameters has stalled the progress of AM. With the number of adjustable variables in printing, materials require extensive, time-consuming testing to determine best printing practices. With the number of FDM materials growing, it is desirable to design an experimental approach to test, evaluate, and predict the best printing parameters. Machine learning methods can identify printing parameter effects on quality indicators, such as surface roughness. The creation of robust models can reduce the costly, time-consuming, and repetitive processing of experimental data, making way for practical applications of FDM parts. The challenge of optimizing these parameters is particularly critical because of the anisotropic properties inherent to the FDM process. While a broad range of printing

variables exists, their impact is most significant on the interlayer adhesion and mechanical strength of the final part, making the development of robust predictive models through machine learning a powerful solution for overcoming this material property limitation.

The layer-by-layer nature of FDM results in anisotropic properties of the product [4]. Anisotropic material exhibits different mechanical properties among different planes and axes, leading to unpredictable material strength and performance [5, 6]. During 3D-printing, layers are held by secondary bonds, which are much weaker and more susceptible to failure than polymeric bonds [7]. These secondary, inter-layer bonds lend to the anisotropic nature and various failure modes associated with 3D-printed parts. However, optimization of FDM parameters can improve interlayer adhesion and reduce the severity of anisotropic properties.

FDM includes variables at every stage, from part geometry, material selection, printing process, and post-print procedures [8]. Researchers have primarily examined the influence of printing process variables on the mechanical properties of printed parts. A literature review by Bakhtiari et al. [9] examined the effects of printing variables on the mechanical behavior of polymer-based FDM parts. The review proposed that the variables with the strongest effects on fatigue performance included printing temperature, infill density, build orientation, layer height, and nozzle diameter. Other variables related to the printing process are raster angle, infill pattern, infill density, and layer height. Below in Figure 1, an example of these variables can be seen in a standard dog-bone specimen geometry.

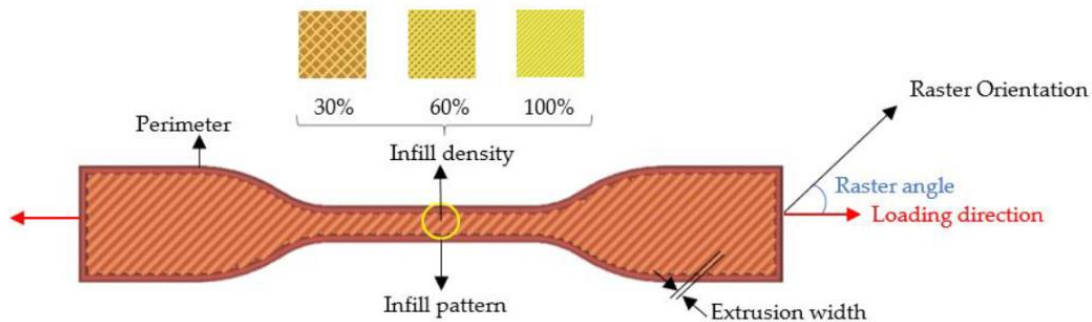


Figure 1: Printing parameters of infill pattern, infill density, body thickness (perimeter), and raster angle [18].

The focus of reducing anisotropic effects of FDM parts is not only limited to improving mechanical strength. Anisotropy also impacts surface roughness on all sides, but namely causing a stair-stepping effect on the planes perpendicular to the build orientation [10]. The surface quality of FDM-produced parts is also related to the mechanical properties of tensile strength and fatigue resistance. In addition to supporting mechanical performance, surface roughness impacts qualitative features like assembly and fitness. For example, in biomedical applications surface roughness determines the validity and usability of printed parts with patients. Smooth surfaces are also necessary to perform proper cleaning and sterilization of potential FDM-produced equipment [11, 12].

Sherif et al. [13] investigated the impacts of printing parameters on PLA 3D-printed parts and found a direct relationship between layer thickness and infill density with surface roughness.

Mendrickv et al. [14] also found that layer height, printing speed, and part orientation impacted surface roughness of PLA FDM parts. Jakupi et al. [15] also indicated layer height, print speed, and infill density as the printing parameters most impactful to surface roughness. Researchers have also used Taguchi arrays to examine combinations of printing parameters and predict surface roughness results. Hasdiansah et al. [16] found specific process variables that reduced surface roughness, while also conducting an ANOVA to identify layer thickness as the most influential parameter. While research has indicated that key parameters like layer thickness can impact surface roughness, testing all printing parameters manually can be expensive and time-consuming.

With the advent of machine learning, data collected from printed specimens has been used to train neural networks. By supplying collected data to machine learning algorithms, researchers can train models to predict the outcome of prints, reducing the time required to determine patterns manually [17, 18, 19]. Combining machine learning with experimental design arrays can expand the analysis of printing parameters and provide insights on a larger scale.

In this study, FDM Nylon 12 specimens were printed according to a Taguchi L54 array with various levels of key printing parameters, including infill pattern, infill density, body thickness, raster angle, and orientation. Post-processing steps of annealing were also investigated. The specimens were analyzed under an optical laser microscope at two specific locations, Site A and Site B, and measured for surface roughness values. Three machine learning algorithms were trained using Random Forest Regression on the individual site datasets and a combined dataset. The relationships between the printing parameters and surface roughness values were assessed through the models, showcasing key correlations within site-specific data, but lacking efficacy with the combined-site model. Further understanding of printing parameter relationships with surface roughness was found through evaluating the correlative matrices, feature importances, mutual information, and ANOVA measures across the models. Ultimately, Body Thickness and Orientation were identified as printing parameters with a statistically significant effect on surface roughness measurements.

## **2. Materials and Methods**

### **2.1 Experimental Design**

The methodological design was created by using Taguchi method L54 array [20]. The Taguchi L54 array allows for three repeated prints for a select parameter combination. This method improves the dataset by providing multiple specimens for a set number of parameters. Evaluating the performance of printing parameters across three identical prints improves the robustness of the dataset.

The L54 array consisted of one parameter with two levels, and five parameters with three levels each. The two-level parameter was annealing, with levels of ‘Yes’ and ‘No.’ The five remaining parameters were directly related to printing parameters available for user editing, namely infill pattern, infill density, body thickness, raster angle, and orientation. The full parameters and levels are described by Table 1 below.

Table 1: Experimental Parameters and Levels

Parameters	Number of Levels	Level Values		
<b>Infill Pattern</b>	3	Solid	Hexagonal	Cross (thick)
<b>Infill Density</b>	3	Max	Mean	Min
<b>Body Thickness</b>	3	Max	Mean	Min
<b>Raster Angle</b>	3	15	45	75
<b>Print Orientation</b>	3	Auto	XY	-XY
<b>Annealing</b>	2	Yes	No	■

The parameter level values are determined by the GrabCAD software available through the Fortus printer [21]. For each material, the range of each variable varies slightly. To standardize the arrays and potentially expand this research to additional materials, levels of ‘Maximum,’ ‘Mean,’ and ‘Minimum’ were chosen for the parameters of infill density and body thickness. The exact values of these vary based on infill pattern. For example, a ‘Solid’ infill pattern will be automatically assigned ‘Maximum’ for infill density, so the Taguchi array must be modified for all ‘Solid’ assignments. Body thickness also has different ranges of values dependent on the infill pattern. The full table of specifications are shown below in Table 2. Further discussion on the remaining printing parameters will take place in the Specimen Preparation section.

Table 2: Printing Parameters Based on Infill Pattern

Infill Pattern		Infill Density		Body Thickness	
		Maximum	1	Maximum	1
		Mean	2	Mean	2
		Minimum	3	Minimum	3
<b>Solid</b>	1	<b>Solid</b>		<b>Solid</b>	
		100	1	0.124	1
		100	2	0.069	2
		100	3	0.014	3
<b>Hexagonal</b>	2	<b>Hexagonal</b>		<b>Hexagonal</b>	
		60%	1	0.122	1
		44%	2	0.083	2
		33%	3	0.042	3
<b>Cross-thick</b>	3	<b>Cross</b>		<b>Cross</b>	
		80%	1	0.122	1
		51%	2	0.082	2
		22%	3	0.042	3

The selected geometry of the experiment was a dental surgical guide, shown below in Figure 2. This geometry was selected for its relatively small size, requiring an average of 0.929 in<sup>3</sup> of model material and 1.143 in<sup>3</sup> support material. Additionally, the complex geometry of the surgical guide offers multiple areas of analysis. The planar features of the surgical entry points were utilized as the areas of surface roughness analysis. In future analyses, the unique curvature of the connecting rod and inner curvatures can be examined for surface roughness discrepancies.

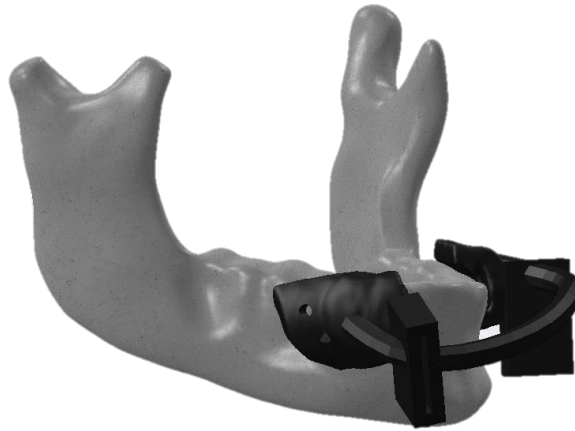


*Figure 2: Mandible surgical guide (black) on CAD jaw model (gray).*

## **2.2 Materials and Equipment**

The specimens were fabricated with the Fortus 450mc industrial printer produced by Stratasys, shown below in Figure 3. The model material, Nylon 12, and the support material, SR-110, were procured from Stratasys. To extrude the filament, nozzle diameters of T16 and T12SR100 were used for the model material and the support material, respectively. Nylon build sheets were also sourced from Stratasys [22, 23, 24].



*Figure 3: Stratasys Fortus450mc Printer [22].*

Annealing post-processing was performed on half of the specimens, totaling 28. According to available research, the suggested annealing process for Nylon 12 filament is between 100°C and 135°C in an annealing oven [25]. Annealing processes have shown positive effects on mechanical properties of tensile and flexural strength. Additionally, the process of annealing requires heating the specimen above the material's glass transition temperature, allowing interfacial bonds to become stronger [26]. The annealing processes were hypothesized to result in lower surface roughness parameters due to increased interlayer bonding. After trialing an annealing process at 130°C for 4 hours and 100°C for 8 hours, the 100°C at 8 hours process was chosen. The 130°C process provided temperatures too high for the unique geometry to tolerate and resulted in warping. The 100°C process allowed annealing to the specimens without dramatically changing the specimen shape.

The support filament was dissolved in a post-processing step using a Support Cleaning Apparatus (SCA-1200) shown in Figure 4 [27]. WaterWorks P400 Soluble Concentrate was procured through Stratasys and used in the SCA tank [28]. To ensure the specimens were fully submerged in the apparatus, thin stainless steel mesh sheets were molded and wrapped around the specimens.



*Figure 4: Support Cleaning Apparatus (SCA-1200) to remove SR-110 filament [27].*

The final instrument used in the experiment was a VK-X1000 from Keyence [29]. The 3D laser scanning microscope was used to analyze surface roughness at two measurement sites on each specimen. Tin foil molds were carefully created to allow the sites to be fixed parallel to the platform. Due to the specimen geometry and the limited focal length of the microscope, only the top planar surfaces of the specimens were possible to analyze in the microscope. The VK-X viewing and analysis software was used to calculate detailed surface roughness measurements.

### **2.3 Specimen Preparation**

The selected geometry is a surgical guide for the mandible, specifically made from an anonymous patient's CT scans. The surgical guide was analyzed and optimized in SolidWorks 2021 to ensure completeness and reduce meshing errors. The geometry was then loaded into the GrabCAD software connected with the Fortus printer and automatically checked for any model errors. Each specimen was set to be fabricated with Nylon 12 model material in a T16 nozzle, and SR-110 support material in a T12SR100 nozzle. The slice height of the model was automatically

determined by the nozzle size, eliminating the potential to examine layer thickness on surface roughness. For the T16 nozzle, the slice height was 0.010 in [30]. The printer also set the chamber temperature and tip temperatures automatically based on the chosen material and could not be edited by user input.

Three identical specimens were placed in the GrabCAD software and adjusted to match the parameters set by the Taguchi array. The first four elements to be adjusted were the infill pattern (style), infill density, body thickness, and raster (infill) angle, as seen in Figure 5. The specific infill styles, or infill patterns, are shown in Figure 6 Figure 6as solid, hexagram, and cross-thick.

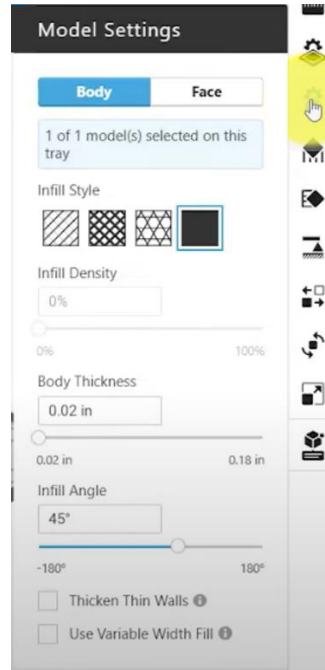


Figure 5: GrabCAD Software Model Settings, showing the variable parameters of infill pattern, infill density, body thickness, and raster angle.

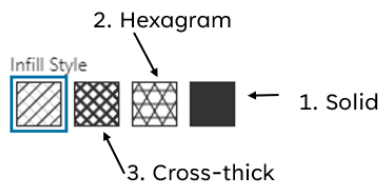


Figure 6: Specific examples of the infill styles used were 1) solid, 2) hexagram, and 3) cross-thick.

The Taguchi L54 array was carefully referenced to select the correct parameter levels for the infill pattern, infill density, body thickness, and raster angle. The Support settings, seen below in Figure 7A, were automatically set to produce ‘SMART’ support styles, which allows for tapered supports that utilize less material [31]. Additionally, the specimens were given three 0.1 in diameter anchors along the plane closest to the build platform, seen in Figure 7B. Nylon 12 has the tendency

to warp and curl, and with the complex geometry chosen, it was found that these anchors stabilized the part during building.

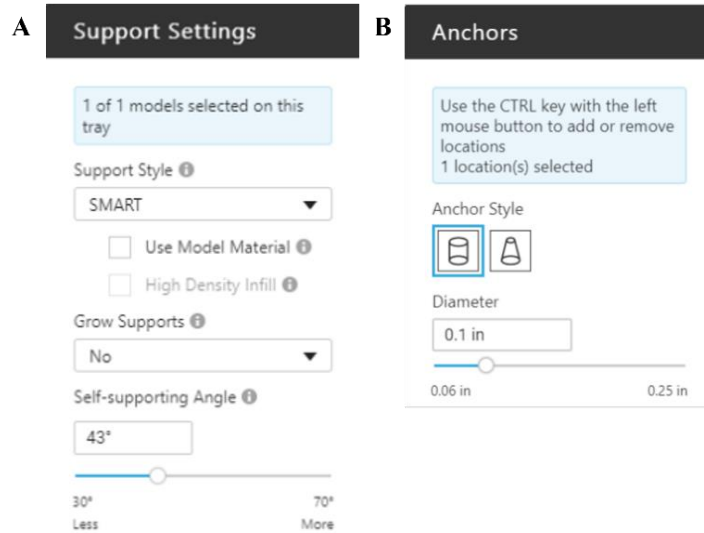


Figure 7: GrabCAD Print Settings for A) Supports and B) Anchors.

Finally, the orientation of the geometry was decided using the Orient settings, seen in Figure 8A. The first orientation was 'Auto', which is a GrabCAD calculated orientation to minimize material usage and time required for a build. The 'Auto' orientation is shown in Figure 8B. The second orientation, referenced as 'XY,' used a reference plane of the 3D geometry to be placed parallel to the build platform. In Figure 8, the geometry has transparent boxes on one of the surgical guide boxes. The top plane of this box was used as the reference plane for orientation, and one of the key measurement sites. The third orientation rotated the 'XY' around the y-axis 180 degrees. The three orientations can be seen below in Figure 8. These three orientations were decided after multiple trials with XZ, YZ, and other orientations that failed to print. These orientations also minimize the amount of model and support material used and reduce the risk of warping effects and disconnection of the print with the build platform.

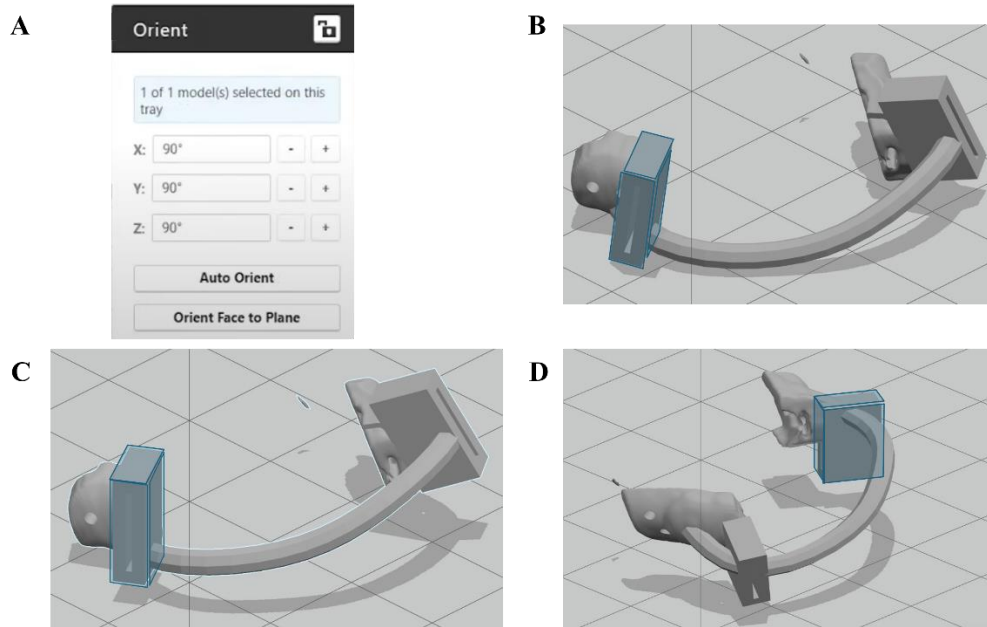


Figure 8: A) Orientation in GrabCAD Print, B) Auto, C) XY, and D) XY-180.

## 2.4 Part Post-processing

After the fabrication, the Fortus printer automatically cooled down. The build sheet was removed from the chamber with the specimens still attached. After the specimens sufficiently cooled to room temperature, they were carefully removed from the build sheet. The image in Figure 9 displays three examples of specimens across the three orientations with support filament still attached. Half of the specimens were placed in an annealing oven to undergo an 8-hour cycle of annealing at 100°C [25].



Figure 9: Printed specimens of the following orientations: A) Auto, B) XY, and C) XY-180.

All the specimens underwent post-processing treatment to dissolve the support filament. The main bulk of the support filament was removed manually, but areas close to or connected to model material were not removed. The Support Cleaning Apparatus (SCA) was fully cleaned and prepared with 11 gallons of fresh water. A full bottle of WaterWorks soluble concentrate, sodium hydroxide, was added to the tank per instructions [32]. The pH of the mixture was checked to ensure a pH around 12, which was required to ensure proper support removal. The specimens were

wrapped in a stainless-steel mesh so they would be fully submerged in the solution, as seen in Figure 10. The specimens were processed in batches of three, corresponding to the three repeated prints in the Taguchi array, to reduce potential specimen mix-up and allow for full support material removal. The SCA automatically heated the solution to 70°C, and a timer was set to run for 4.5 hours for each cleaning cycle. Afterwards, the specimens were removed and inspected for residual support material. If material was detected, the specimens were submerged for an additional 1 hour in the solution. The specimens were patted dry with paper towels and air dried for multiple days before being analyzed.



*Figure 10: Example of specimens wrapped in stainless steel mesh bags to be placed in the SCA.*

## **2.5 Surface Roughness Measurement**

After post-processing steps were completed, the specimens were analyzed with the VK-X microscope. The two sites selected are shown below in Figure 11. Site A and Site B were chosen due to the planar surfaces that could be easily positioned to be parallel with the microscope viewing platform. Site A is a feature that is parallel to the build platform during printing for the XY and XY-180 orientations, while Site B is never parallel to the build platform. Additionally, Site A and Site B are some of the last pieces of the model to be built during Auto and XY orientations. However, both sites are oriented upside-down in the XY-180 orientation, and are surrounded by support material, as shown before in Figure 9. These sites offer the most variation and easiest location when viewing under the microscope.

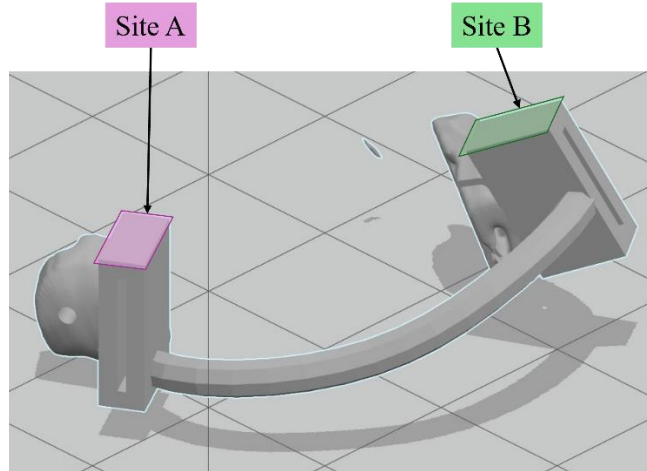


Figure 11: Site A and Site B location specified on the 3D model of geometry.

The specimens were positioned under the microscope using tin foil to secure in place. The tin foil molds were able to hold the specimens in positions where each site would be parallel to the viewing platform, increasing the accuracy of the surface roughness measurements. In Figure 12A, the setup for Site A can be seen. In Figure 12B, a closer example of the tin foil arrangement can be seen for Site B.

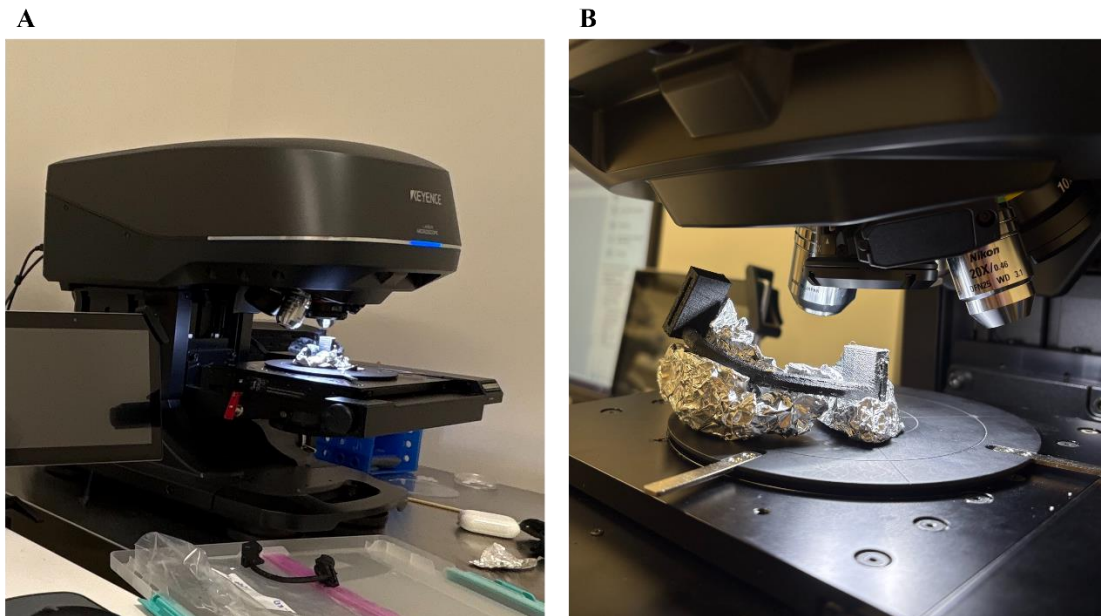
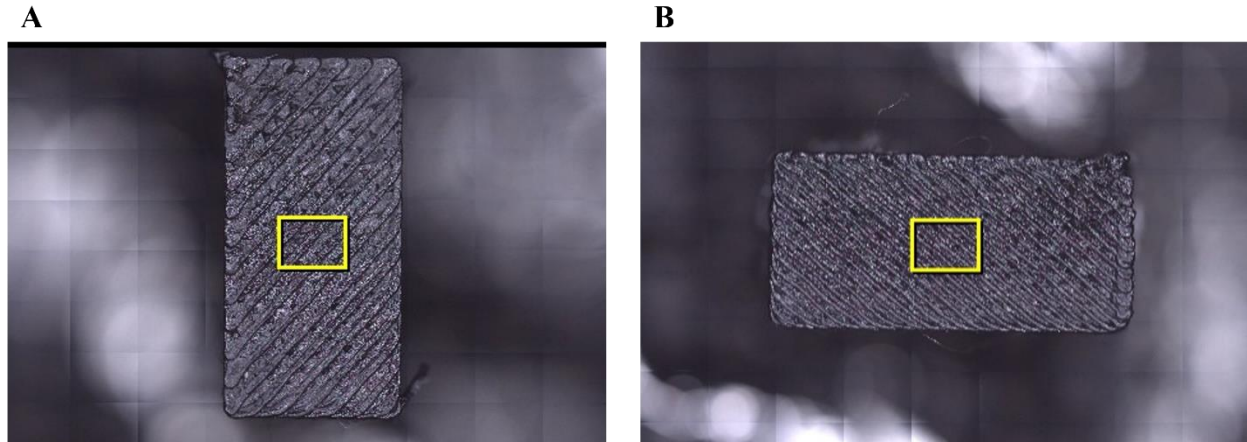


Figure 12: Arrangement of specimens under VK-X for A) Site A and B) Site B.

A field-of-view image was taken of both sites prior to the surface roughness assessments. In Figure 13 below, Specimen #17 is shown in both Site A and Site B. In Figure 13A, Site A is oriented vertically, while Figure 13B shows Site B horizontally. Due to the unique geometry of the model and the limited room of the VK-X, Site B was collected with a 90° counterclockwise rotation. The yellow boxes in the center of each image showcase the area of measurement. To

standardize the measurements across all specimens and sites, the approximate center of each site was used as the measurement area. The average specimen area evaluated was  $0.0583 \text{ cm}^2$  across both sites.

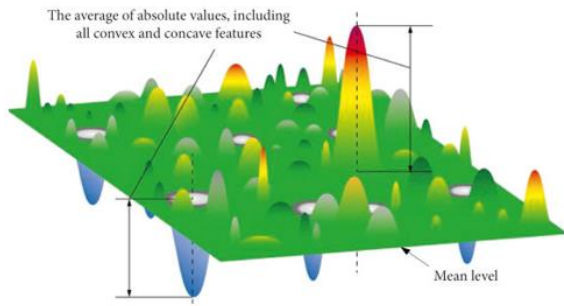


*Figure 13: Specimen #17 showed at A) Site A and B) Site B.*

For each site, six surface area roughness measurements were collected [33]. Three of these measurements, the arithmetical mean height (Sa), maximum height (Sz), and root mean square height (Sq), were parameters focused on height changes in the surface [34]. The arithmetic mean peak curvature (Spc) measurement was a feature parameter. The developed interfacial ratio area (Sdr) was a hybrid parameter, while the texture aspect ratio (Str) was a spatial parameter [35].

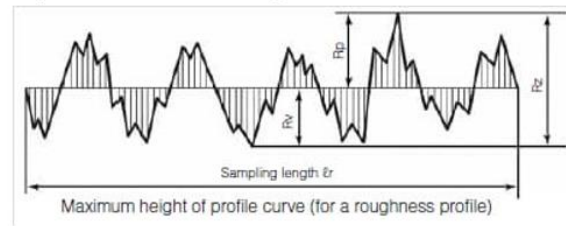
The arithmetical mean height, Sa, calculates the difference between the height of a surface feature and the arithmetical mean of the surface. All changes in surface height of the selected area were assessed to find the average distance to the mean surface plane. A larger Sa value indicates more variance in the roughness of the selected specimen [36]. The maximum height, Sz, was found by summing the lowest pit depth with the largest peak height within the selected area. A large Sz value indicates a notable change in the surface roughness [37]. The Sq value uses the root mean square of height values across the selected area. The Sq calculation finds a standard deviation of surface height changes from the mean surface plane [38]. In Figure 14A-C, graphical representations can be seen for Sa, Sz, and Sq, respectively.

**A) Sa - arithmetical mean height**



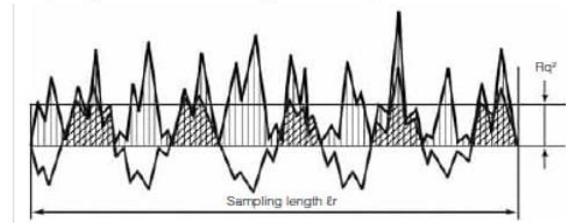
$$Sa = \frac{1}{A} \iint_A |Z(x,y)| dx dy$$

**B) Sz - maximum height**



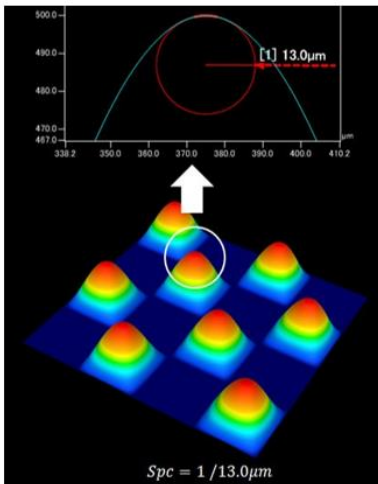
$$Sz = Sp + Sv$$

**C) Sq - root mean square height**



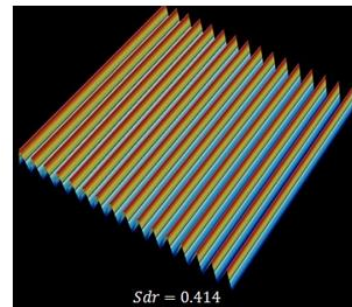
$$Sq = \sqrt{\left(\frac{1}{A}\right) \iint_A Z^2(x,y) dx dy}$$

**D) Spc - arithmetic mean peak curvature**



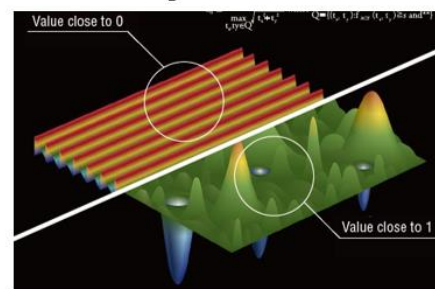
$$Spc = \left(-\frac{1}{2}\right) \left(\frac{1}{n}\right) \sum_{k=1}^n \left(\frac{\partial^2 z(x,y)}{\partial x^2} + \frac{\partial^2 z(x,y)}{\partial y^2}\right)$$

**E) Sdr - developed interfacial ratio**



$$Sdr = \left(\frac{1}{A}\right) \left[ \iint_A \left( \sqrt{1 + \left(\frac{\partial z(x,y)}{\partial x}\right)^2 + \left(\frac{\partial z(x,y)}{\partial y}\right)^2} - 1 \right) dx dy \right]$$

**F) Str - texture aspect ratio**



$$f_{ACF}(t_x, t_y) = \frac{\iint_A z(x,y)z(x-t_x, y-t_y) dx dy}{\iint_A z(x,y)z(x,y) dx dy}$$

Figure 14: Surface roughness measurements for A) Sa, B) Sz, C) Sq, D) Spc, E) Sdr, and F) Str [33-41].

The arithmetic mean peak curvature, or Spc, value represents the average of the principal curvature of peaks on the surface. A large Spc value indicates pointed shapes on the surface, and a

smaller value indicates rounded shapes [39]. The developed interfacial ratio, Sdr value, identifies any slope existing within the measured area due to additional surface features. A flat plane will have a Sdr value of 0, and the value will increase with additional surface features [40]. Finally, the texture aspect ratio, Str, value measures the uniformity of surface texture. A Str value greater than 0.5 indicates uniform texture in all directions of the surface measured. A value lower than 0.3 suggests there is a strong directional structure or lay on the surface [41]. In Figure 14D-F, graphical representations can be seen for Spc, Sdr, and Str, respectively.

## 2.6 Machine Learning Methodology

The data was collected and stored for each specimen, with Site A and Site B each having 54 data sets. These datasets included the six surface roughness parameters calculated from the VK-X1000 microscope. For the scope of this paper, the images were not evaluated extensively; rather, the primary focus was on the numerical calculations. Each dataset was combined with the Taguchi L54 array to include the six categorical features of print parameters. Initially, the Site A and Site B datasets were assessed separately and later combined to evaluate potential correlations.

The data was evaluated for potential outliers or missing data points. In total, six rows of data were removed from the overall dataset, reducing the specimen number to 48. OneHotEncoder was used to identify the categorical features of the printing parameters. The data was then split into an 80% training set and a 20% test set. When Site A and Site B datasets were combined, the site identification was added as a categorical feature. The combination of data allows the model to identify potential differences between the two sites within the same specimen group.

To evaluate the data, Random Forest Regressor was chosen as the base model. Because of the high variability between printing parameter features and surface roughness targets, the Random Forest model was chosen to handle complex and non-linear data relationships [42, 43]. Random Forest Regressor models were trained with training data for Site A, Site B, and combined datasets specifying between a 'Site' feature. To improve the performance of the RF models, a cross-validation grid search was performed to identify the best hyperparameters available. The grid search did not result in significant changes in the model performance, but the parameters identified were used.

The RF models were utilized with 100 estimators and a random state of 42. The models were tested by predicting values for target values based on the features of the test set. To evaluate effectiveness, Mean Squared Error (MSE), Mean Absolute Error (MAE), and R-squared (R<sup>2</sup>) values were calculated for each model. The results of the models were evaluated by analyzing correlation matrices, feature importance, mutual information scores, and ANOVA [44].

## 3. Results & Discussion

### 3.1 Raw Data Characteristics

The surface roughness data was found to vary between the two collection sites. A summary of the surface roughness measurements used as target data in the machine learning models can be seen in Table 3 below. For both locations, the maximum height (Sz) jumped significantly from the

mean height (Sa). Site B had a consistently larger surface roughness measurements compared to Site A, but generally showed smaller standard deviations, showing more consistency than Site A. This phenomenon may be described by Site A’s ability to be parallel to the build sheet during printing in two orientations, whereas Site B is never parallel to the build sheet in any orientation.

Table 3: Summary of Surface Roughness Measurements for Cleaned Data of Site A and Site B

	Site A				Site B			
	Min	Max	Avg	Std Dev	Min	Max	Avg	Std Dev
<b>Sa - Mean Height (µm)</b>	12.50	363.99	54.66	56.42	40.20	109.10	71.96	18.62
<b>Sz - Max height (µm)</b>	122.83	1635.11	500.32	306.94	373.88	1120.56	674.16	175.01
<b>Sq - RMS height (µm)</b>	15.64	415.95	70.13	66.92	50.69	158.65	90.32	24.26
<b>Spc - mean peak curvature (1/mm)</b>	94.20	1806.65	742.23	545.61	843.51	2427.50	1503.51	365.16
<b>Sdr - interfacial ratio area</b>	0.04	7.86	1.49	1.53	1.02	8.63	3.43	1.94
<b>Str - texture aspect ratio</b>	0.07	0.59	0.23	0.13	0.05	0.61	0.16	0.12

### 3.2 Machine Learning Model Performance

Three models were trained using Random Forest Regression, each corresponding to datasets of Site A, Site B, and combined sites. The model evaluation scores can be seen in Table 4. Out of the MSE and MAE evaluations, Site A data had the lowest scores, while the combined dataset had the highest. Site A therefore showed the best predictive accuracy when comparing test data and prediction data. For the R2 score, Site A data also performed the best, with the highest score of 0.879, showing the model’s ability to identify variance between the target variables.

Table 4: Summary of MSE, MAE, and R2 Scores for RF Models

	<b>Mean Squared Error (MSE)</b>	<b>Mean Absolute Error (MAE)</b>	<b>R-squared (R2)</b>
<b>Site A Model</b>	2117.4489	21.7828	0.8790
<b>Site B Model</b>	7094.8067	40.1725	0.6906
<b>Combined Model</b>	14346.93	54.6007	0.4966

### 3.3 Correlation Matrices

Correlation matrices in machine learning represent the correlation between all combinations of variables for a dataset. Negative correlations indicate that increasing one value

will decrease the other. Positive correlations indicate that increasing one value will also increase the other value [45]. The correlation matrices offer a broad overview of potential data relationships. The correlation matrix for Site A is shown below in Figure 15.

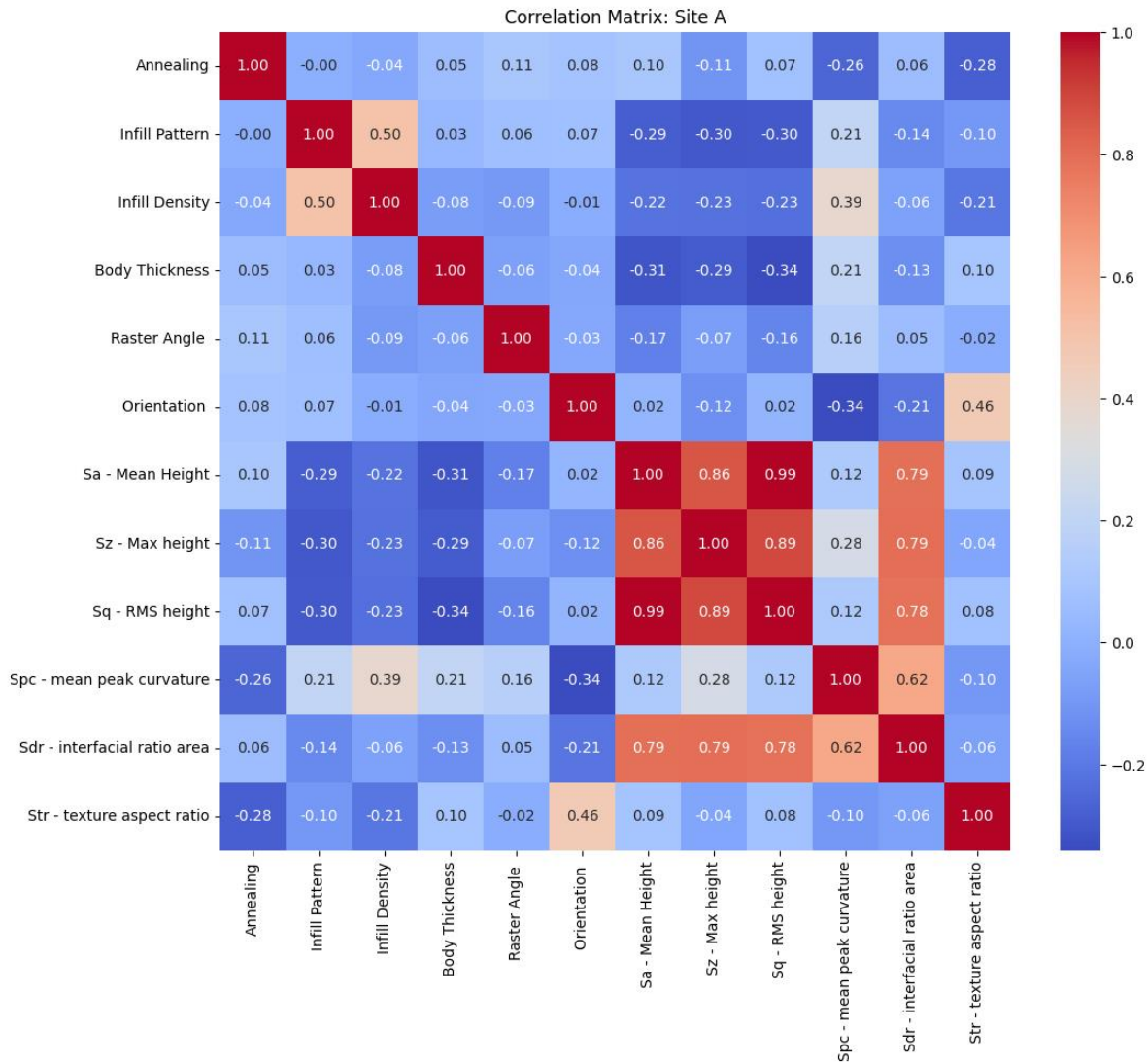


Figure 15: Correlation Matrix for Site A, showing negative correlations in dark blue and positive correlations in dark red.

Site A shows that the printing parameters of infill pattern and body thickness have a negative correlation with the height-related target variables of mean height (Sa), maximum height (Sz), and RMS height (Sq), with the largest value being -0.34 between body thickness and RMS height (Sq). The correlation suggests that increasing the values of body thickness will reduce the surface roughness. In addition to body thickness, orientation has the strongest negative correlation of -0.34 on mean peak curvature (Spc). This value suggests that the XY-180 orientation is correlated with smoother peaks on Site A’s surface. Annealing also demonstrates a negative correlation of -0.26 with Spc, as well as -0.28 with texture aspect ratio (Str).

Site A also presents some moderate positive correlations. Between infill density and Spc, a value of 0.39 was observed, which indicates that infill densities of a lower percent may lead to pointier surface features. Additionally, there is a positive correlation of 0.46 between orientation and Str, suggesting that the XY and XY-180 orientations provided more uniform surface textures. Considering that Site A is parallel to the build sheet when in these two orientations, this correlation is expected.

Site A showed consistent negative correlations between the printing parameters of infill pattern, body thickness, and orientation with surface roughness measurements. Site B, in contrast, only indicated a negative correlation with body thickness across nearly all surface roughness measurements. Site B also demonstrated negative correlations of -0.30 between annealing and Spc, and -0.27 between annealing and Sz. These relationships can be viewed in Figure 16 below.

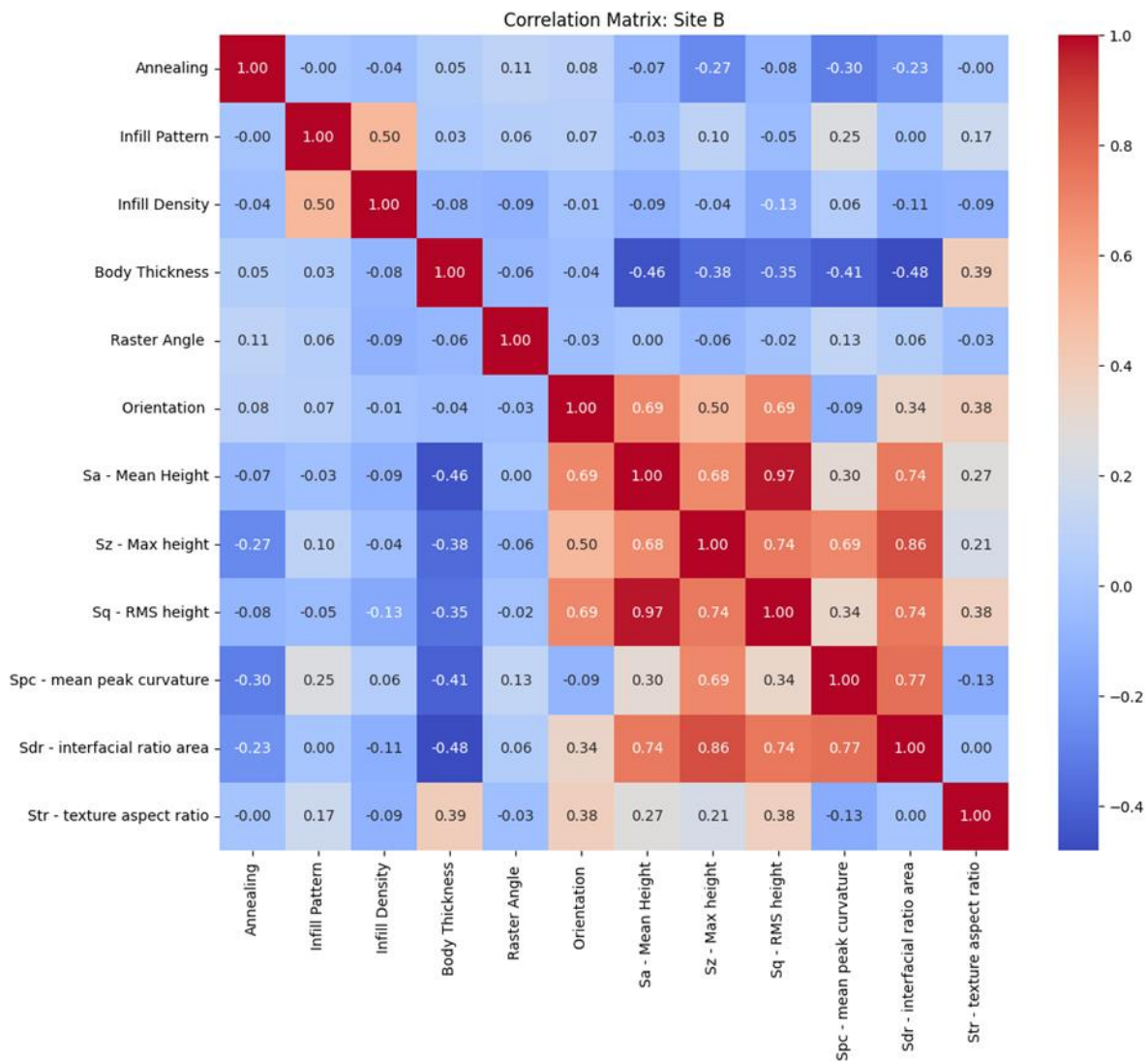


Figure 16: Correlation Matrix for Site B, showing negative correlations in dark blue and positive correlations in dark red.

In contrast to Site A, Site B presented more positive than negative correlations with orientation across most surface roughness measurements. Site B demonstrated a weak negative correlation of -0.09 between orientation and Spc. Orientation had the largest positive correlation values of 0.69 between Sa and Sq. Positive correlation values between orientation and Sz were 0.50 and Str were 0.38. Body thickness also showed a connection between Str, with a value of 0.39.

The two matrices show that both Site A and B demonstrate positive correlations with infill pattern and orientation. As the infill pattern 'increases' in the Taguchi array, it progresses from Solid – 1, Hexagram – 2, and Cross-thin – 3. Higher values of infill pattern, namely the more sparse and less dense patterns, create sharper surfaces, indicated by the Spc. However, both sites present negative correlations with infill pattern and Sa. While the surfaces may become pointier as the infill pattern becomes less solid, the average height of the surface peaks is reduced. Similarly, as the orientation progress from Auto – 1, XY – 2, and XY-180 – 3, the Str increases, leading to a less uniform surface.

Both sites show negative correlation with body thickness and surface roughness height measurements of Sa, Sz, and Sq. As the body thickness parameters increase from Maximum – 1, Mean – 2, and Minimum – 3, the surface roughness generally improves. The same trend can be seen for annealing, which progress from Yes – 1 to No – 2, and suggests that annealing worsens the surface quality.

To further understand similarities and differences between the sites, the RF model was run on a combined dataset, where the sites were added as additional categorical features. The correlation matrix for the combined dataset was considerably weaker than the individual sets, showing few similarities between the measurements from both sites. However, the observed positive and negative correlations mentioned previously, namely the orientation, body thickness, and infill pattern, were also observed in the combined correlation matrix, shown below in Figure 17.

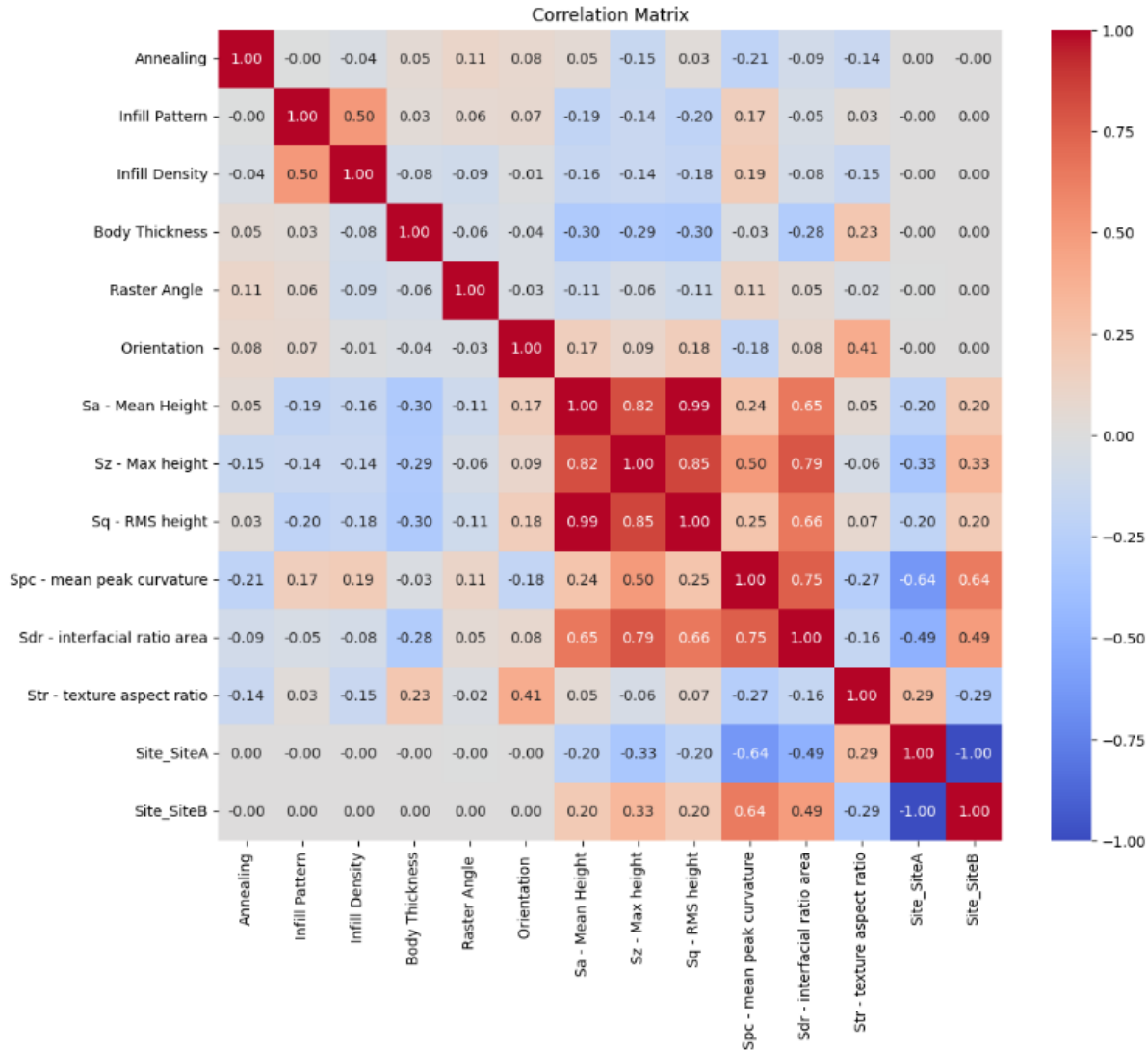


Figure 17: Combined Site A and Site B correlation matrix, showing orientation, body thickness, and infill pattern impact surface roughness measurements.

### 3.4 Feature Importance

The feature importance of Site A and Site B provides critical understanding and interpretation of the printing parameter effects on surface roughness parameters. While Site A displayed more correlations, Site B showed higher feature importance. In Figure 18 below, both sites show the same top three feature importances of orientation, infill pattern, and body thickness. Orientation has a stronger importance for Site B, which may be explained by the irregular and non-parallel positioning of the site during printing orientations. The remaining printing parameters drop steeply in importance for Site B, while Site A maintains relative importance scores. This indicates that the correlations found for Site B had a stronger influence on the target variables of surface roughness.

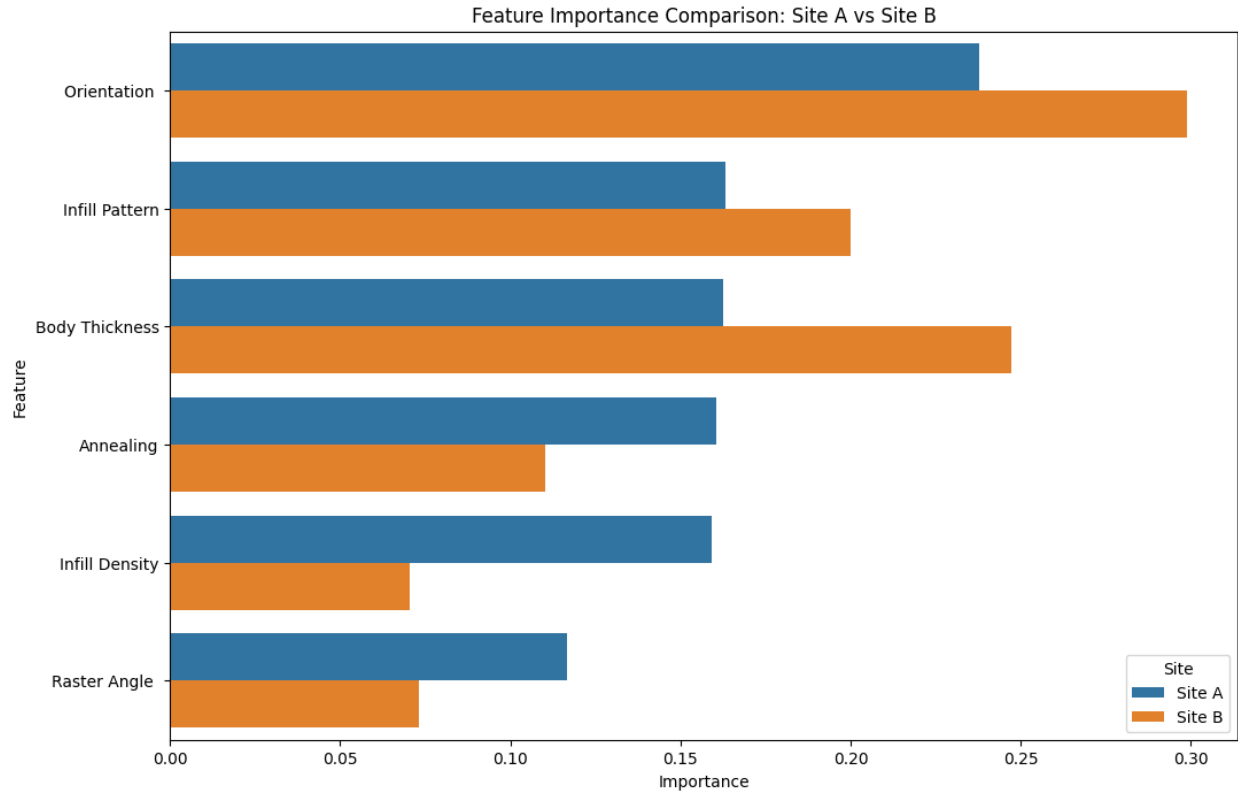


Figure 18: Feature Importance Comparison for Site A and Site B Models, with orientation, infill pattern, and body thickness as the most important.

### 3.5 Mutual Information

The Mutual Information analysis was performed separately for each site and broken down by categorical levels. This analysis provides deeper insights into the dependencies between the printing parameters as features and surface roughness values as target variables. The Taguchi array consisted of numerous parameters across various levels. The specific parameters and values that impacted the surface roughness values can be optimized for future applications.

In Figure 19 below, the Mutual Information comparison graph can be seen. The top categorical indicator for both sites was orientation. Specifically, the orientation levels of Auto and XY-180 are shown to have the highest mean mutual information values across both sites. Body thickness, specifically the minimum value, has high mutual information values for both Sites, but is the second highest score for Site B. The annealing parameter shows mean mutual information values higher for Site A than Site B, suggesting that it is a better predictor for surface roughness predictors in Site A.

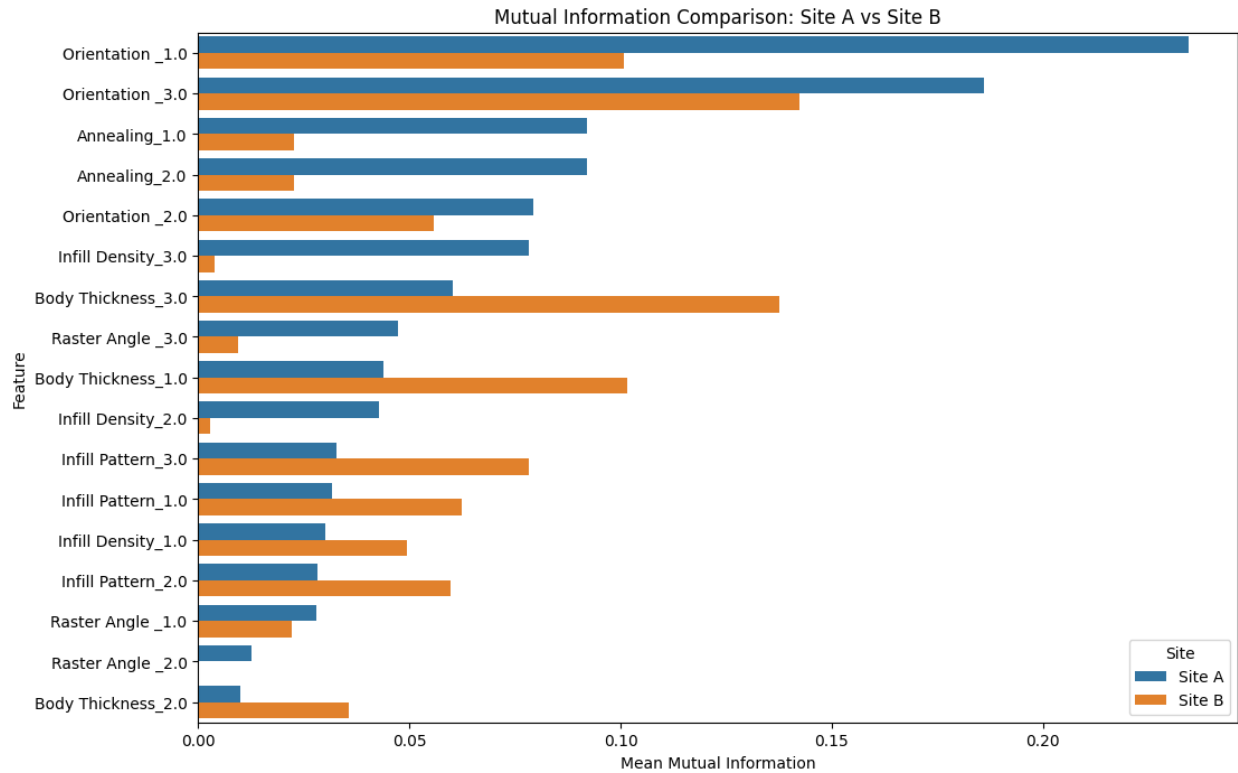


Figure 19: Mean Mutual Information scores for Site A and Site B, organized by Site A importance, showing similarities between orientation, but differences in impact across other features.

Further discrepancies between the two sites and their mean mutual information are evident with the infill density level of minimum, or level 3. For Site A, this feature is the sixth highest in mean mutual value, but the fifteenth for Site B. Conversely, Site B shows a high mean mutual value for body thickness level of Minimum, but it does not rank as high for Site A. In general, body thickness plays a larger role in predicting target values for Site B, while infill density plays a larger role for Site A. Infill pattern and raster angle ranks lower for both sites.

### 3.6 ANOVA Comparison

To gain further clarity on the relationship between Site A and Site B, an Analysis of Variance (ANOVA) was conducted. The means of target variables across the categories of each feature of each site were compared and placed in a heat map. In Figure 20 below, the difference between p-values for ANOVA calculations for specific features and target variables is shown in a heatmap. Negative values suggest that Site B had a much larger value than Site A, suggesting the relevance of a specific feature for Site A. Higher values show that Site A had a larger value than Site B, suggesting Site B finds that feature more important.

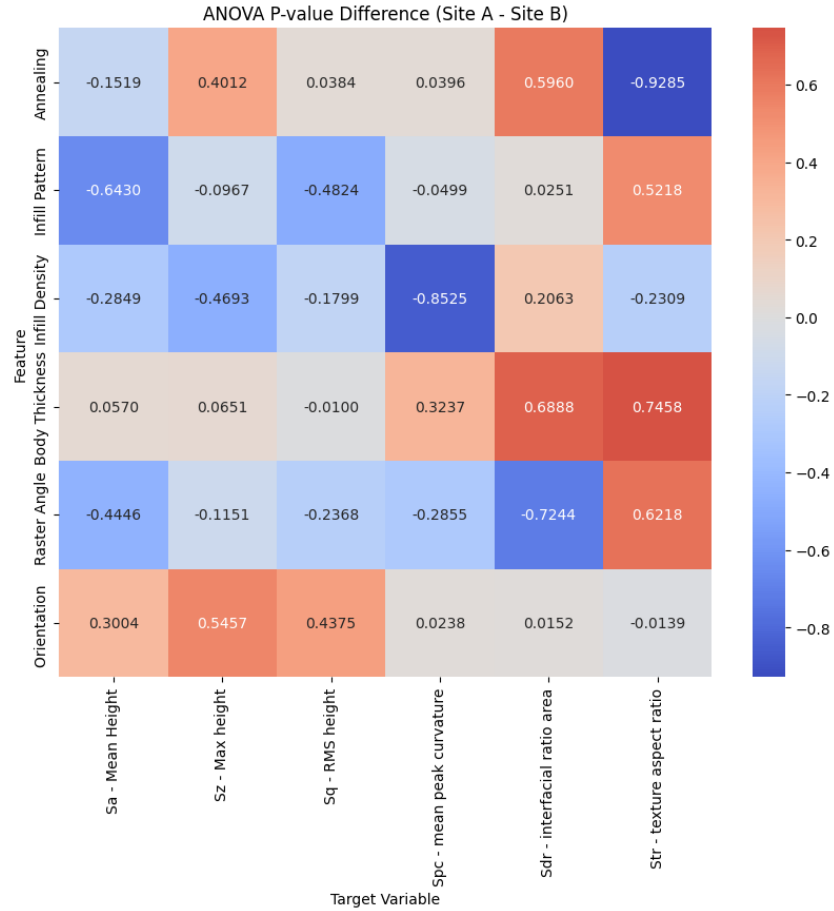


Figure 20: ANOVA comparison of P-values for Site A and Site B.

The critical P-values calculated by ANOVA for each site are shown below in Table 5. Body thickness and orientation show p-values less than 0.05 across both sites, meaning that these features have a statistically significant impact on the target variables of surface roughness measurements.

Table 5: Statistically Significant P-values for Site A and Site B.

Feature	Target	P-value Site A	P-value Site B
<b>Annealing</b>	Spc - mean peak curvature		0.0363
<b>Infill Pattern</b>	Spc - mean peak curvature	0.0035	
	Sq - RMS height	0.0489	
<b>Infill Density</b>	Spc - mean peak curvature	0.0068	
<b>Body Thickness</b>	Sa - Mean Height		0.0052
	Sz - Max height		0.0318
	Sq - RMS	0.0430	
	Spc - mean peak curvature		0.0091
	Sdr - interfacial ratio area		0.0024
<b>Orientation</b>	Spc - mean peak curvature	0.0378	0.0140

	Sdr - interfacial ratio area		0.0349
	Str - texture aspect ratio	0.0013	0.0152

#### 4. Conclusion

This work aimed to draw connections to the complex relationships between FDM printing parameters and resulting surface roughness measurements across two collection sites on the same part geometry. Through a rigorous machine learning approach, the study successfully developed predictive models and unveiled critical insights into how printing variables influence surface quality.

A key finding was the pronounced difference in surface roughness characteristics between Site A and Site B, with Site B consistently exhibiting rougher surfaces. This disparity is likely attributable to Site A's ability to maintain parallelism with the build sheet in two orientations, a condition not met by Site B in any orientation. The Random Forest Regression model demonstrated superior predictive accuracy for Site A's surface roughness, a R2 of 0.879, compared to Site B and to the combined dataset. The significant drop in model performance and correlation strength when combining data from both sites underscores the variability of surface roughness in angled and non-parallel build surfaces.

Further analysis through correlation matrices, feature importance, mutual information, and ANOVA revealed distinct site-specific influences of printing parameters. While orientation, body thickness, and infill pattern consistently emerged as the most impactful features across both sites, their relative importance varied. Orientation showed a stronger influence at Site B, which can be attributed to its non-parallel printing positions. Conversely, infill density, specifically at the 'Minimum' level, was a more significant predictor for Site A. Body thickness, also at the 'Minimum' level, held greater predictive power for Site B. Annealing was identified as a more effective predictor for worsening surface sharpness, by increasing surface measurements across both sites. The ANOVA comparison further solidified these findings, with statistically significant p-values less than 0.05 for infill pattern and body thickness across both sites, indicating their critical role in optimization of surface roughness.

This paper highlights the ability to identify key relationships between variables, levels, and numerous target data points of the FDM process by utilizing a Random Forest model. However, further research can be conducted to explore more machine learning methods to find more accurate model prediction and stronger relationships between the two data collection sites. Additionally, the incorporation of other materials as categorical features can contribute to the growing body of research on material behavior in FDM. In conclusion, this study provides valuable insights into optimizing surface quality for FDM Nylon 12 parts by highlighting the statistical significance of printing parameters. The findings emphasize that effective process optimization requires an understanding of localized changes in surface roughness. This research contributes to the growing body of knowledge in additive manufacturing, offering practical implications for manufacturers seeking to achieve desired surface finishes and enhance the reliability of FDM-produced components.

## 5. Acknowledgement

This research is based on the work funded by the University of North Florida Foundation.

## 6. References

- 
- [1] Grand View Research. (2023). 3D Printing Market Size, Share & Trends Analysis Report, 2030. Available: <https://www.grandviewresearch.com/industry-analysis/3d-printing-industry-analysis>.
- [2] M. E. Hernandez Korner *et al*, "Cost Model Framework for Pieces Additively Manufactured in Fused Deposition Modeling for Low to Medium Batches," *3D Printing and Additive Manufacturing*, vol. 11, (1), pp. 287–298, 2024, DOI: 10.1089/3dp.2022.0044.
- [3] V. Mishra *et al*, "Recent advances in fused deposition modeling Fused Deposition Modeling based additive manufacturing of thermoplastic composite structures: A review," *J Thermoplast Compos*, vol. 36, (7), pp. 3094–3132, 2023. DOI: 10.1177/08927057221102857.
- [4] S.-H. Ahn, M. Montero, D. Odell, S. Roundy, and P. K. Wright, "Anisotropic material properties of fused deposition modeling ABS," *Rapid prototyping journal*, vol. 8, no. 4, pp. 248–257, 2002, DOI: 10.1108/13552540210441166
- [5] John Case, Lord Chilver, and Carl T.F. Ross, "5 - Analysis of stress and strain," in *Strength of Materials and Structures*, Fourth Edition. Butterworth-Heinemann, 1999, pp. 94–151, DOI: 10.1016/B978-034071920-6/50009-1
- [6] A. R. Torrado and D. A. Roberson, "Failure Analysis and Anisotropy Evaluation of 3D-Printed Tensile Test Specimens of Different Geometries and Print Raster Patterns," *Journal of Failure Analysis and Prevention*, vol. 16, no. 1, pp. 154–164, 2016, doi: 10.1007/s11668-016-0067-4
- [7] Y. Lyu *et al*, "Architecture of covalent bonds between filament layers to enhance performance of 3D printing biodegradable polymer blends," *Polym. Test.*, vol. 106, pp. 107456, 2022, DOI: 10.1016/j.polymertesting.2021.107456.
- [8] D. Popescu *et al*, "FDM process parameters influence over the mechanical properties of polymer specimens: A review," *Polym. Test.*, vol. 69, pp. 157–166, 2018, DOI: 10.1016/j.polymertesting.2018.05.020.
- [9] H. Bakhtiari, M. Aamir, and M. Tolouei-Rad, "Effect of 3D Printing Parameters on the Fatigue Properties of Parts Manufactured by Fused Filament Fabrication: A Review," *Applied sciences*, vol. 13, no. 2, pp. 904–, 2023, DOI: 10.3390/app13020904
- [10] P. Ficzer, "Surface Anisotropy on 3D Printed Parts," *Periodica polytechnica. Mechanical engineering - Mašinstroenie*, vol. 68, no. 3, pp. 272–277, 2024, doi: 10.3311/PPme.37770
- [11] M. A. Alghauli *et al*, "Impact of 3D printing orientation on accuracy, properties, cost, and time efficiency of additively manufactured dental models: a systematic review," *Bmc Oral Health*, vol. 24, (1), pp. 1550–16, 2024, DOI: 10.1186/s12903-024-05365-5.
- [12] L. Frizziero *et al*, "Heat Sterilization Effects on Polymeric, FDM-Optimized Orthopedic Cutting Guide for Surgical Procedures," *J Funct Biomater*, vol. 12, (4), pp. 63, 2021, DOI: 10.3390/jfb12040063.
- [13] M. Sherif, S. Mekhiel, A. S. Elmesalamy, and H. Mahmoud, "Investigation of FDM Process Parameters and their Interactions on Surface Roughness of PLA 3D Printed Parts," *Journal of physics. Conference series*, vol. 3058, no. 1, p. 12017, 2025, doi: 10.1088/1742-6596/3058/1/012017
- [14] R. Mendricky and D. Fris, "Analysis of the Accuracy and the Surface Roughness of FDM/FFF Technology and Optimisation of Process Parameters," *Tehnički vjesnik*, vol. 27, no. 4, pp. 1166–1173, 2020, doi: 10.17559/TV-20190320142210
- [15] K. Jakupi, V. Dukovski, and G. Hodolli, "Surface Roughness Modeling of Material Extrusion PLA Flat Surfaces," *International Journal of Polymer Science*, vol. 2023, Art. no. 8844626, 2023, doi: 10.1155/2023/8844626
- [16] H. Hasdiansah, R. I. Yaqin, P. Priistiansyah, M. L. Umar, and B. H. Priyambodo, "FDM-3D printing parameter optimization using taguchi approach on surface roughness of thermoplastic polyurethane parts," *International journal on interactive design and manufacturing*, vol. 17, no. 6, pp. 3011–3024, 2023, doi: 10.1007/s12008-023-01304-w
- [17] R. Ratnavel, S. Viswanath, J. Subramanian, V. K. Selvaraj, V. Prahasam, and S. Siddharth, "Predicting the Optimal Input Parameters for the Desired Print Quality Using Machine Learning," *Micromachines (Basel)*, vol. 13, no. 12, pp. 2231–, 2022, DOI: 10.3390/mi13122231

- 
- [18] M. R. N. Mohamed *et al.*, "Exploring the process-structure-property relationship of nylon aramid 3D printed composites and parameter optimization using supervised machine learning techniques," *Journal of engineered fibers and fabrics*, vol. 20, Art. no. 15589250241293883, 2025, DOI: 10.1177/15589250241293883
- [19] D. Ege, S. Sertturk, B. Acarkan, and A. Ademoglu, "Machine learning models to predict the relationship between printing parameters and tensile strength of 3D Poly (lactic acid) scaffolds for tissue engineering applications," *Biomedical physics & engineering express*, vol. 9, no. 6, Art. no. 065014, 2023, DOI: 10.1088/2057-1976/acf581
- [20] J. M. Cimbala. Taguchi orthogonal arrays. Taguchi orthogonal arrays. 2014. Available: [https://www.me.psu.edu/cimbala/me345/Lectures/Taguchi\\_orthogonal\\_arrays.pdf](https://www.me.psu.edu/cimbala/me345/Lectures/Taguchi_orthogonal_arrays.pdf).
- [21] Stratasys Inc., "GrabCAD Print Software," 2025. Available: <https://grabcad.com/print/>.
- [22] Stratasys. *Fortus 450mc*. Available: [https://www.stratasys.com/siteassets/3d-printers/printer-catalog/fdm-printers/fortus-450mc/h2-model-updates/pss\\_fdm\\_fortus450mc\\_0924a.pdf?v=4ab5d9](https://www.stratasys.com/siteassets/3d-printers/printer-catalog/fdm-printers/fortus-450mc/h2-model-updates/pss_fdm_fortus450mc_0924a.pdf?v=4ab5d9).
- [23] Stratasys, "FDM Nylon 12 Data Sheet," 2021. Available: [https://www.stratasys.com/siteassets/materials/materials-catalog/fdm-materials/nylon-12/mds\\_fdm\\_nylon-12\\_0921a.pdf](https://www.stratasys.com/siteassets/materials/materials-catalog/fdm-materials/nylon-12/mds_fdm_nylon-12_0921a.pdf).
- [24] *Sheet Bundle, Nylon .02x16x18.5, 20*. Available: <https://hub.stratasys.com/>
- [25] I. Ferreira *et al.*, "Study of the annealing influence on the mechanical performance of PA12 and PA12 fibre reinforced FFF printed specimens," *Rapid Prototyping J*, vol. 26, (10), pp. 1761–1770, 2020, DOI: 10.1108/RPJ-10-2019-0278.
- [26] M. Adamson and B. Eslami, "Post-Processing PEEK 3D-Printed Parts: Experimental Investigation of Annealing on Microscale and Macroscale Properties," *Polymers*, vol. 17, no. 6, Art. no. 744, 2025, DOI: 10.3390/polym17060744
- [27] E. Miller, "Getting to Know PADT: Support Cleaning Apparatus (SCA) Manufacturing and Support - PADT," 2017. Available: <https://www.padtinc.com/2017/07/26/getting-to-know-padt-support-cleaning-apparatus-sca-manufacturing-and-support/>.
- [28] *Waterworks/P400 Soluble Concentrate*. Available: <https://hub.stratasys.com/s/product/waterworksp400-soluble-concentrate/01t0Y000009xh6LQAQ?printerKey=7489483>.
- [29] Keyence Corporation. *Keyence Vx Series*.
- [30] "FDM best practice - nylon 12." Available: [https://advancedtek.com/wp-content/uploads/2016/08/Best\\_Practice\\_-\\_FDM\\_Nylon12\\_-\\_Web\\_-\\_English\\_-\\_12-2015.pdf](https://advancedtek.com/wp-content/uploads/2016/08/Best_Practice_-_FDM_Nylon12_-_Web_-_English_-_12-2015.pdf).
- [31] "3D Printing Best Practices | Stratasys GrabCAD Support," Available: <https://support.stratasys.com/en/Software/GrabCAD-Print/Tips-Guides-and-FAQs/3D-printing-best-practices#support>.
- [32] ORYX Additive, "Best Practices Guide for Soluble Support Removal," 2018. Available: <https://irp-cdn.multiscreensite.com/c35696bb/files/uploaded/SCA-Best-Practices-2018-06-05V2.pdf>.
- [33] D. J. Whitehouse, *Surfaces and their measurement*, 1st ed. London: HPS, 2002.
- [34] T. Liu, J. Wu, J. Lei, X. Wang, B. Zhang, and S. Zhang, "Multifeature Extraction of Three-Dimensional Topography of Carbon Steel Specimen during Fatigue Process," *Advances in materials science and engineering*, vol. 2021, no. 1, Art. no. 6680855, 2021, doi: 10.1155/2021/6680855
- [35] "What Is Surface Area Roughness? | Introduction To Roughness | KEYENCE America," *Keyence*, 2025. Available: <https://www.keyence.com/ss/products/microscope/roughness/surface/>.
- [36] "Sa (Arithmetical Mean Height) | Area Roughness Parameters | Introduction to Roughness | KEYENCE America," *Keyence*, 2025. Available: <https://www.keyence.com/ss/products/microscope/roughness/surface/parameters.jsp>.
- [37] "Sz (Maximum Height) | Area Roughness Parameters | Introduction to Roughness | KEYENCE America," *Keyence*, 2025. Available: <https://www.keyence.com/ss/products/microscope/roughness/surface/sz-maximum-height.jsp>.
- [38] "Sq (Root Mean Square Height) | Area Roughness Parameters | Introduction to Roughness | KEYENCE America," *Keyence*, 2025. Available: <https://www.keyence.com/ss/products/microscope/roughness/surface/sq-root-mean-square-height.jsp>.

- 
- [39] "Spc (Arithmetic Mean Peak Curvature) | Area Roughness Parameters | Introduction to Roughness | KEYENCE America," *Keyence*, 2025. Available: <https://www.keyence.com/ss/products/microscope/roughness/surface/spc-arithmetic-mean-peak-curvature.jsp>.
- [40] "Sdr (Developed Interfacial Area Ratio) | Area Roughness Parameters | Introduction to Roughness | KEYENCE America," *Keyence*, 2025. Available: <https://www.keyence.com/ss/products/microscope/roughness/surface/sdr-developed-interfacial-area-ratio.jsp>.
- [41] "Sal (Auto-Correlation Length) | Area Roughness Parameters | Introduction to Roughness | KEYENCE America," *Keyence*, 2025. Available: <https://www.keyence.com/ss/products/microscope/roughness/surface/sal-auto-correlation-length.jsp>.
- [42] A. Panico, A. Corvi, L. Collini, and C. Sciancalepore, "Multi objective optimization of FDM 3D printing parameters set via design of experiments and machine learning algorithms," *Scientific reports*, vol. 15, no. 1, Art. no. 16753, 2025, DOI: 10.1038/s41598-025-01016-z
- [43] X. Shan, C. Gao, J. H. Rao, M. Wu, M. Yan, and Y. Bi, "Experimental Study and Random Forest Machine Learning of Surface Roughness for a Typical Laser Powder Bed Fusion Al Alloy," *Metals (Basel)*, vol. 14, no. 10, Art. no. 1148, 2024, DOI: 10.3390/met14101148
- [44] Bonaccorso G. *Machine Learning Algorithms: Reference Guide for Popular Algorithms for Data Science and Machine Learning*. 1st edition. Packt; 2017.
- [45] B. Gregorutti, B. Michel, and P. Saint-Pierre, "Correlation and variable importance in random forests," *Statistics and computing*, vol. 27, no. 3, pp. 659–678, 2017, DOI: 10.1007/s11222-016-9646-1